

An Analytical and Experimental Investigation of a Jet Pipe Controlled Electropneumatic Actuator

Paul D. Henri, John M. Hollerbach, *Fellow, IEEE*, and Ali Nahvi

Abstract—An analytical and experimental investigation of a jet pipe controlled electropneumatic servoactuator designed for use in the Utah/MIT dextrous hand (UMDH) has been performed. An accurate dynamic model has been developed and verified which includes detailed representation of the jet pipe element, orifice areas and fluid flows. The effects and modeling of hysteresis in the jet pipe are discussed. Actuator saturation is shown to be an obstacle in achieving high bandwidth. Theoretical and experimental results are presented for frequency response and time-domain force tracking.

Index Terms—Actuators, pneumatic actuators, robot hands.

I. INTRODUCTION

IN RECENT YEARS, much effort has been devoted to the design, construction and control of articulated, multi-fingered robotic hands. The development and use of dextrous hands is an enormously complicated affair involving the close integration of many sub-areas of research including mechanism design, actuation system design, control theory, tactile sensing, grasp planning, kinematic calibration and telemanipulation [1], [12], [16], [25]. Careful study of the individual components that comprise such advanced systems is required if one is to gain a better understanding of the nature of machine dexterity [14].

Since actuator capabilities are perhaps the single most important determinant of manipulator performance [11], [15], it is no surprise that a large amount of research effort has been focused on the study of actuators and their performance within robotic systems. The three main actuation systems in robotics are electromagnetic, hydraulic, and pneumatic. Hydraulic actuators have by far the highest force to mass ratio, and have been successfully employed in robot manipulators such as the Sarcos Dextrous Arm [13]. Some drawbacks in the use of hydraulics are the necessity for a hydraulic pump and inevitable oil leakage, which is not desirable in a multi-fingered hand. Electric motors are very convenient force sources, but are fundamentally limited by low force to mass [11]. New integral gear motors can alleviate this low force to some extent, at the cost of response speed and nonlinear

gear dynamics. Pneumatic actuators are intermediate in force to mass between hydraulic and electromagnetic actuators. Compared to hydraulics, they are lower-cost, cleaner, safer in case of hose rupture, inherently more compliant because of gas compressibility, and have less friction because some leakage of air is allowed. Compared to electromagnetics, the 32-actuator pneumatic package for the Utah/MIT Dextrous Hand is far more compact than would be a comparable electric motor package and has better response.

Each actuator type represents a nonlinear dynamical system, which poses its own challenges for modeling and control. In the case of pneumatics, the compressibility and flow of air require a model-based control in order to achieve a high-bandwidth and smooth motion. This paper investigates the static and dynamic characteristics of the jet pipe controlled pneumatic actuator designed for use in the Utah/MIT Dextrous Hand (UMDH) [16]. The jet pipe electropneumatic servovalve was especially designed for this hand for high performance, as opposed to alternatives such as spool or poppet valves. The key is low moving mass, because the jet pipe is magnetically deflected for control, at the expense of extra air leakage. A similar type of valve is also employed in the hydraulic Sarcos Dextrous Arm.

To date, little work has been done on jet pipe valve controlled actuators. McLain *et al.* [20] developed a dynamic model for a hydraulic version of the actuator studied in this paper. A similar study was performed by Boulet *et al.* [6] with linearized valve and fluid dynamics for a different hydraulic actuator; analysis and control of limit cycles in this actuator were considered by Mouget and Hayward [21]. Both these groups included a static hysteresis model based on a method described in [8], although they did not include results on the effectiveness of the hysteresis model in predicting minor loops. Jacobsen *et al.* [15] performed tests on an early two-stage version of the actuator examined here, and employed a simplified nonlinear model with mixed results.

Most of the early work in pneumatic actuators studied two-stage, four-way spool valves; pneumatic or hydraulic examples are found in most fluid power textbooks [2], [5]. Ben-Dov and Salcudean [3] designed a pneumatic hand controller employing a flapper servovalve. Traditionally, linear transfer functions were used to model pneumatic systems about the mid-stroke operating point [7], [26]. More recently, Liu *et al.* [19] used a state-space method to produce a linearized model valid for several operating points. Shearer [27] performed a digital simulation of a Coulomb-damped hydraulic servosystem using a model with nonlinear valve characteristics.

Manuscript received January 17, 1996; revised April 2, 1998. This paper was supported by the Natural Sciences and Engineering Research Council (NSERC) Network Centers of Excellence Institute for Robotics and Intelligent Systems (IRIS), the NSERC/Canadian Institute for Advanced Research (CIAR) Industrial Chair in Robotics, and an NSERC Postgraduate Scholarship. This paper was recommended for publication by Associate Editor V. Hayward and Editor A. Goldenberg upon evaluation of the reviewers' comments.

P. D. Henri is with Bell-Northern Research Ltd., Ottawa, Ont. K1Y 4H7, Canada.

J. M. Hollerbach and A. Nahvi are with the University of Utah, Salt Lake City, UT 84112 USA.

Publisher Item Identifier S 1042-296X(98)05015-0.

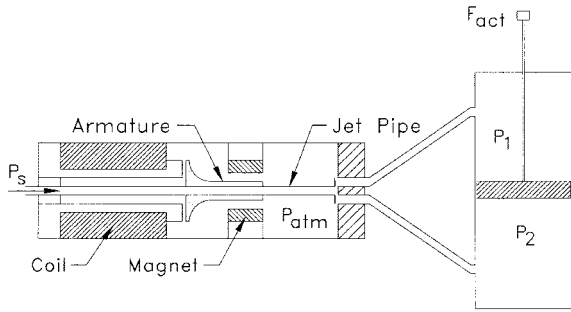


Fig. 1. Schematic diagram of actuator.

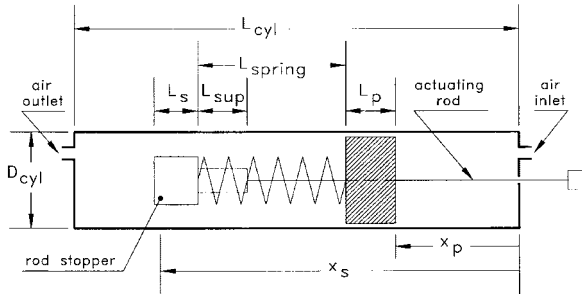


Fig. 2. Schematic diagram of piston/cylinder assembly.

TABLE I
A DESCRIPTION OF SOME PARAMETERS

Parameter	Description	Value
A_p	Piston area	1.24 cm^2
D_{jp}	Orifice diameter	0.9652 mm
P_s	Supply pressure	550 kPa
Stroke	Actuator movement range	5.08 cm

This paper presents a nonlinear model describing the jet pipe element, orifice areas and fluid flows. The effects and modeling of hysteresis are discussed with examples of minor loop trajectories. The performance of the actuator under closed-loop force control is examined with results indicating that a high bandwidth is achievable.

II. ACTUATOR MODEL

A. System Description

The electro-pneumatic actuator consists of a single-stage, jet pipe valve attached to a glass cylinder, housing a low-stiction graphite piston and steel rod (Fig. 1). Current passing through the coil controls the position of the jet pipe, which directs a high pressure air flow toward the orifices to each side of the piston. The pressure difference across the piston produces a force that is applied against a stopper on the end of the actuating rod (Fig. 2). Table I shows the values of some major parameters. The following sections examine each component of the actuator, and outline the relevant equations in the model (Fig. 3).

The current driver is a first order low pass system with a corner frequency of 1122 Hz, much higher than the actuator bandwidth. Thus, we start by modeling the jet pipe.

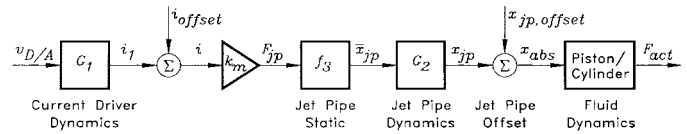


Fig. 3. Block diagram of actuator model.

B. Jet Pipe

The jet pipe consists of a small diameter stainless-steel tube fixed at one end passing between a pair of permanent magnets. The jet pipe is magnetized by the coil, and interacts with the perpendicular flux lines of the permanent magnet such that the effective force on the jet pipe tip F_{jp} is proportional to current i :

$$F_{jp} = k_m i \quad (1)$$

where k_m is the force constant. This force acts in a direction perpendicular to both the jet pipe axis and a line joining the permanent magnets.

Originally, it was thought to model the jet pipe as a second-order linear system to capture the first bending mode. Instead, the frequency and step-response tests of Section III-A indicate a static nonlinearity followed by an independent third-order linear system (Fig. 3). The static nonlinearity function f_3 relates F_{jp} to static tip position \bar{x}_{jp}

$$\bar{x}_{jp} = f_3(F_{jp}). \quad (2)$$

The third-order linear system is

$$G_2(s) = \frac{X_{jp}(s)}{\bar{X}_{jp}(s)} = \left(\frac{\omega_1}{s + \omega_1} \right) \left(\frac{\omega_2^2}{s^2 + 2\zeta_2\omega_2s + \omega_2^2} \right) \quad (3)$$

where ω_1 and ω_2 are breakpoint frequencies, and ζ_2 is the damping ratio. We don't have a precise explanation why it is third order. A possible justification might be a second order model for the jet pipe and a first order model for the nonlinear seal between jet pipe and valve body.

Significant hysteresis was found in the static position versus current relationship. An attempt to model the hysteresis according to the model of Frame *et al.* [8], which was employed in previous jet-pipe studies [6], [20], failed in predicting the minor loop trajectories [10]. In theory, the static nonlinearity f_3 could be used to model the hysteresis effect. As explained later, because of the lack of a good hysteresis model, the function f_3 is taken to be the midpoint line of the experimentally obtained x_{jp} versus F_{jp} curve shown in Fig. 6(b).

To account for any misalignment between the jet pipe origin and the receiver plate center, an offset $x_{jp,offset}$ is added to yield the position $x_{jp,abs}$ of the jet pipe tip from the receiver plate center

$$x_{jp,abs} = x_{jp} + x_{jp,offset}. \quad (4)$$

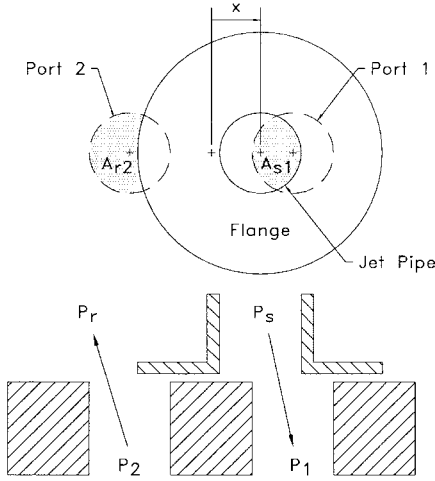


Fig. 4. Orifice areas.

C. Orifice Areas

The orifice areas through which fluid flows in or out of a control port are calculated from the geometrical overlap of the jet pipe and control ports (Fig. 4). The small clearance between the jet pipe tip and the receiver plate does not appear explicitly in the model, but rather is lumped into the discharge coefficient. The control ports of the receiver plate are of the same diameter as the jet pipe exit area and are spaced one diameter apart. The jet pipe tip has a flange which serves to cover the opposite control port when the pipe is directed away from center. The diameter of the flange is three times the diameter of the jet pipe exit area; thus the flange just covers the control ports when the pipe is centered. Port 1 is connected to the charging side of the piston and port 2 to the venting side. P_s and P_r are the supply and return pressures. The return area A_{r1} for port 1 and the supply area A_{s2} for port 2 are both covered by the jet pipe tip flange and hence are zero. See [9] for the equations describing the orifice areas.

D. Flow Equations

Assuming the flow processes are adiabatic, the mass flow rates through the orifices are governed by the following equations [2], [5], [28]

$$\dot{m} = \begin{cases} C_d A \left(\frac{P_u}{\sqrt{T_u}} \right) C_1 & \text{for } \left(\frac{P_d}{P_u} \right) \leq r_c \\ C_d A \left(\frac{P_u}{\sqrt{T_u}} \right) C_2 f_2 & \text{for } \left(\frac{P_d}{P_u} \right) > r_c \end{cases}$$

$$r_c = \left(\frac{P_d}{P_u} \right)_{cr} = \left(\frac{2}{\gamma + 1} \right)^{\frac{\gamma}{\gamma - 1}}$$

$$C_1 = \sqrt{\frac{\gamma}{R} \left(\frac{2}{\gamma + 1} \right)^{\frac{\gamma + 1}{\gamma - 1}}}, \quad C_2 = \sqrt{\frac{\gamma}{R} \left(\frac{2}{\gamma - 1} \right)}$$

$$f_2 = \sqrt{\left(\frac{P_d}{P_u} \right)^{\frac{2}{\gamma}} - \left(\frac{P_d}{P_u} \right)^{\frac{\gamma + 1}{\gamma}}} \quad (5)$$

where P_u and P_d are the upstream and downstream pressures, T_u is the upstream temperature, $\gamma = 1.4$ is the isentropic

exponent for air, $R = 287 \text{ j/kg} \cdot \text{K}$ is the gas constant for air, $r_c = 0.528$ is the critical pressure ratio for air at which the flow changes from subsonic to sonic, A is the orifice area, and C_d is the orifice discharge coefficient.

The actuator is designed to be slightly “leaky,” allowing a small flow between the chambers past the position. This leakage area is ring shaped and is long relative to its opening width, indicating that the discharge coefficient should be a function of pressure ratio [2], instead of a constant as is the case with the other orifices. Therefore, the discharge coefficient for the leakage past the piston area A_{lpp} is

$$C_{d,lpp} = C_{dm} \left(\frac{P_d}{P_u} \right) + C_{db} \quad (6)$$

where C_{dm} and C_{db} are constants.

The net mass flow rates for chambers 1 and 2 are

$$\dot{m}_1 = \dot{m}_{s1} - \dot{m}_{r1} - \dot{m}_{lpp} \quad (7)$$

$$\dot{m}_2 = \dot{m}_{s2} - \dot{m}_{r2} + \dot{m}_{lpp} \quad (8)$$

where the orifice area is A_{s1} for \dot{m}_{s1} and A_{r1} for \dot{m}_{r1} , and the positive sense for \dot{m}_{lpp} is from chamber 1 to chamber 2.

The net volumetric flow rate Q_i for each chamber $i = 1, 2$ is simply the mass flow rate divided by the density

$$Q_i = \frac{\dot{m}_i}{\rho_i} \quad (9)$$

where the density ρ_i is obtained from the ideal gas law

$$\rho_i = \frac{P_i}{RT_i} \quad (10)$$

Due to the moderate pressures and temperatures involved, the model can be simplified by assuming that temperatures T_i do not vary appreciably from their nominal values and can be assumed constant. A study by Kawakami *et al.* [17] revealed little difference in response of a pneumatic cylinder model whether the pneumatic processes are assumed isothermal or adiabatic. In reality, the flow processes lie somewhere between isothermal and isentropic.

In an adiabatic flow, we have

$$P_i v_i^\gamma = \text{constant} \quad (11)$$

where v_i is the specific volume of air in chamber i . Differentiating and simplifying, the rate of change of pressure \dot{P}_i in each chamber is

$$\dot{P}_i = \frac{\gamma P_i}{V_i} (Q_i - \dot{V}_i) \quad (12)$$

where V_i is the volume of chamber i .

E. Piston Dynamics

The piston inside the cylinder is spring loaded and slides along the actuator rod between the rod stopper and the end of the cylinder (Fig. 2). This arrangement maintains residual tension in the tendons when the system is un-pressurized, preventing tendon misalignment. When the pressure difference across the piston is sufficiently high, the spring becomes fully compressed and the piston contacts the rod stopper. The spring

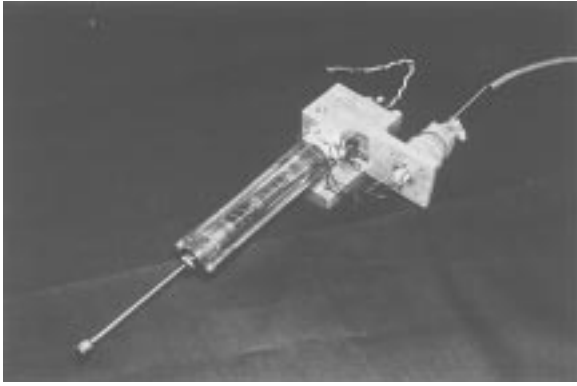


Fig. 5. Apparatus for measuring jet pipe position.

has a low spring constant, and hence the piston contacts the rod stopper for all but extremely low actuator forces.

Friction between the graphite piston and glass cylinder is small [16] and is further reduced by the lubricating effect of the air flow past the piston. Friction between the rod and cylinder seal is assumed insignificant as well. The dynamics of the load are expected to dominate those of the lightweight, low-friction graphite piston, which means that for all practical purposes the piston dynamics can be neglected. The actuator can only pull, not push, so for the case when $P_1 > P_2$ the actuator force is

$$F_{\text{act}} = A_p(P_1 - P_2) \quad (13)$$

where A_p is the piston area; otherwise the force is equal to the spring force.

III. SYSTEM IDENTIFICATION

A. Jet Pipe

Static Characteristics: To measure the position of the jet pipe, a miniature HP HEMT-6000 light emitting diode was attached to the tip of the jet pipe, and its position was sensed by a SiTek J1L position sensitive detector (PSD). The apparatus (Fig. 5) was calibrated by deflecting the jet pipe tip with a probe attached to a micrometer plunger and recording the corresponding output of the PSD.

By slowly ramping the current up and down until the position saturated, the characteristic major hysteresis loop was obtained [Fig. 6(a)]. To determine the source of the hysteresis, mechanical testing was performed on the jet pipe by applying forces directly on the jet pipe tip via hanging masses. Due to limitations in the experimental apparatus, it was possible to deflect the jet pipe downwards only. From the position/current curve [Fig. 6(a)] and the left half of the position/force curve [Fig. 6(b)] it was possible to derive the bottom half of the force/current curve [Fig. 6(c)]. The force/current curve was reasonably assumed to be symmetric for positive force and current, permitting the derivation of the right half of the position/force curve. Since the effects of hysteresis are not directly accounted for in the system model, the nonlinear function $f_3(F_{jp})$ in (2) is simply the midpoint line of the position/force curve.

The force/current curve [Fig. 6(a)] shows only a slight amount of hysteresis and is linear within the actuator's rated

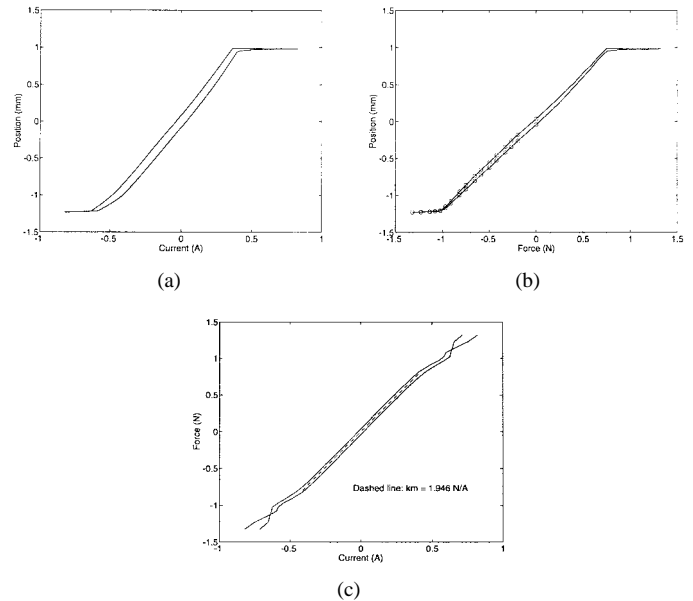


Fig. 6. (a) Jet pipe position versus current. (b) Jet pipe position versus tip force. (c) Jet pipe tip force versus current.

current limits of ± 0.4 A. The best fit for this operating range gives a force constant $k_m = 1.946$ N/A, and is indicated by the dashed line. It is surprising that the force/current relationship of the coil is not the sole source of hysteresis—Fig. 6(b) clearly shows that there exists a significant amount of hysteresis in the position/force relationship as well. A possible explanation is that the jet pipe is not fixed to the valve body in a cantilevered fashion, but rather is held in a sleeve containing some type of seal or o-ring with nonlinear characteristics.

The separation between the halves of the jet pipe position/current major hysteresis loop is almost constant in the operating range at ≈ 0.16 mm. Therefore, comparing the distance between the midpoint line and the major loop, 0.08 mm, to the jet pipe operating range, 1 mm, gives a hysteresis of approximately 8%.

Dynamic Characteristics: A swept sine frequency response test was performed to identify the parameters of the third-order jet pipe model presented in Section II-B. Fig. 7 shows that a third-order model fits the data well for frequencies below ≈ 700 Hz. The strange behavior of the system above 700 Hz can likely be attributed to saturation of the current amplifier. Referring to (3), the identified parameters are: $\omega_1 = 973.9$ rad/s (155.0 Hz), $\omega_2 = 1856.7$ rad/s (295.5 Hz), and $\zeta_2 = 0.019$.

A step response test confirmed that the jet pipe is highly underdamped with a rise time of 0.002 s and a 5% settling time of 0.07 s [9].

B. Actuator Response

The experimental apparatus to obtain the actuator force/current characteristics consisted of a compact Entran ELF-TC500-100 force sensor, which was rigidly fixed to a plate attached to UMDH actuator package (Fig. 8).

Static Characteristics: Fig. 9(a) shows the actuator major hysteresis loop, which was obtained by slowly ramping the

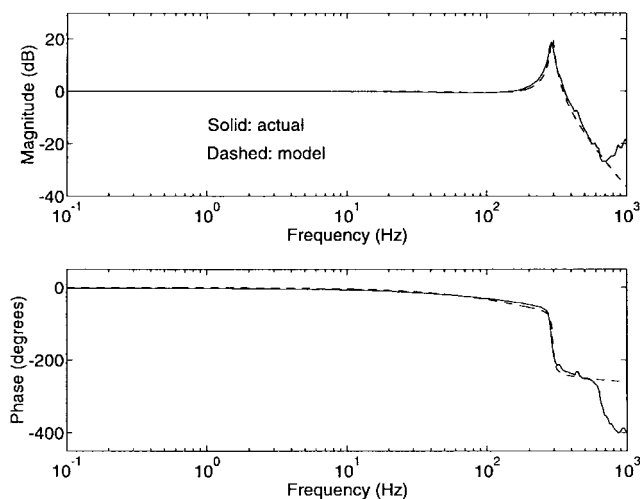


Fig. 7. Jet pipe frequency response: $X_{jp}(j\omega)/\bar{X}_{jp}(j\omega)$.



Fig. 8. Apparatus used to measure actuator force.

current up and down to the force saturation points. The procedure was automated by using the Condor real-time control system [23], driving Data Translation 12-b D/A and 16-b A/D boards. This test was repeated for several different rod stopper positions, and confirmed that the static actuator force does not depend on the relative volume of the cylinder chambers. The model data uses the jet pipe position/current major hysteresis loop data of Fig. 6(a), and is indicated by a dashed line. Using the actuator force/current data and the jet pipe position/current data, the actuator force/jet pipe position curve was derived [Fig. 9(b)].

The remaining parameters, the orifice discharge coefficients and the receiver plate offset, were identified by minimizing the sum of the squared errors between the experimental and theoretical actuator force/current major hysteresis loops. The model used the experimental jet pipe major hysteresis loop data to calculate the supply and return orifice areas. The correct model parameters were obtained using the multidimensional downhill simplex method [24]. The piston leakage area A_{lpp} could not be obtained directly but was obtained in combination with the discharge coefficient slope and offset. Referring to (4)–(6), the identified parameters are: $x_{jp,offset} = 0.099$

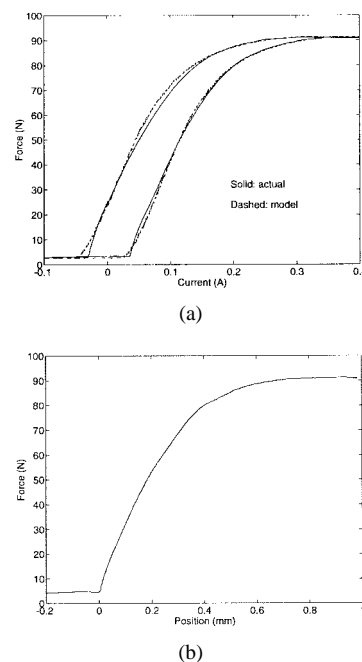


Fig. 9. (a) Actuator force versus current. (b) Actuator force versus jet pipe position.

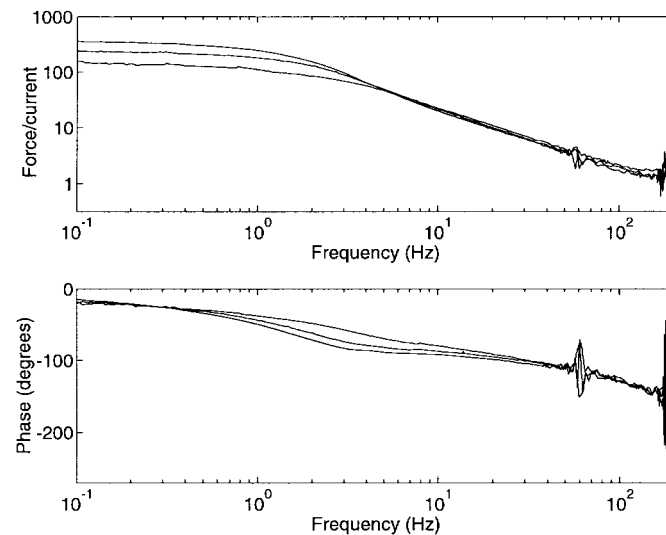


Fig. 10. Actuator open-loop force/current frequency response for varying mean currents. Amplitude = 0.01 A.

mm, $C_d = 0.696$, and $C_{d,lpp}A_{lpp} = -0.0475(P_2/P_1) + 0.0971 \text{ mm}^2$. More details can be found in [9].

Dynamic Characteristics Several open-loop frequency response tests were performed on the actuator with currents of varying amplitude and mean to observe the degree of nonlinearity in the system. These tests qualitatively show the overall system response and provide a rough estimate for the time constant of the system. Fig. 10 shows the force/current response for varying mean currents, with the piston at approximately the mid-stroke position ($x_s = 54$ mm). Fig. 11 shows similar data for varying amplitudes. The results show a low bandwidth ranging from 0.8 to 2.8 Hz, which increases slightly for both mean current and amplitude. This bandwidth is in agreement with the linear analysis in

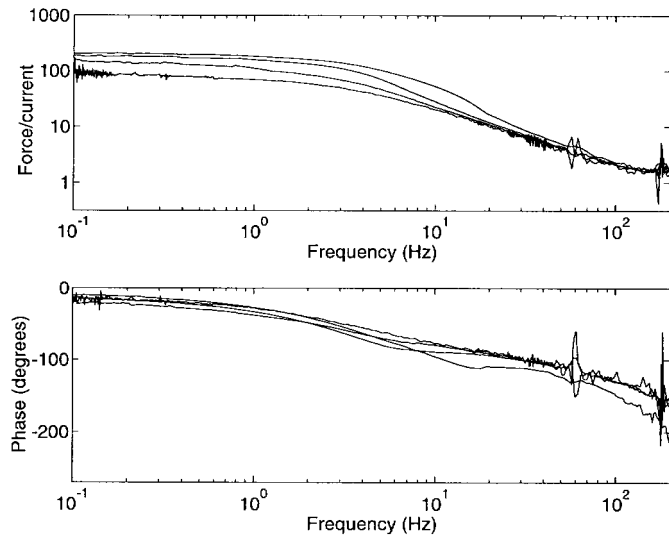


Fig. 11. Actuator open-loop force/current frequency response for varying amplitude currents. Mean = 0.15 A.

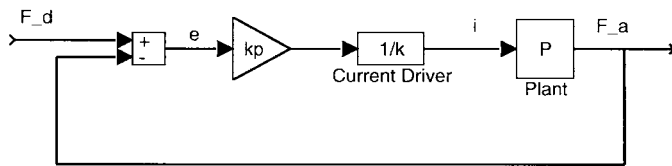


Fig. 12. Proportional feedback controller. F_d and F_a are desired and actual actuator forces, respectively.

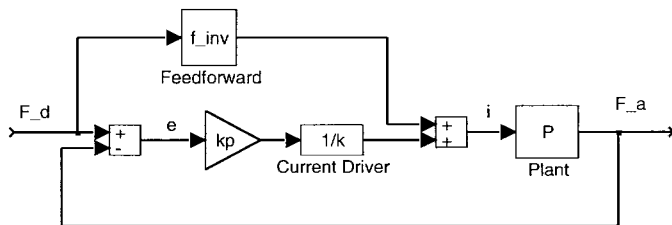


Fig. 13. Feedforward control.

Section V-B. After linearizing the actuator model about an operating point corresponding to an output force of 45 N, the system is shown to act as a first-order, low-pass filter with a corner frequency of 2.3 Hz.

The shape of the curves indicates a nonlinear system that acts as a low-pass filter, approaching an integrator. Systems of this type require some type of feedback to linearize their response and overcome the adverse effects of hysteresis.

IV. CLOSED-LOOP CONTROL

The performance of the actuator and the model was examined by implementing several different digital controllers using the Condor real-time control system. Figs. 12 and 13 show the control block diagram using proportional feedback and feedforward control respectively. k_p represents proportional gain, and k represents the force/current ratio in the static case. f^{-1} is the nonlinear midpoint line of force/current data in Fig. 9(a), i.e., $\bar{i} = f^{-1}(F_d)$. Therefore, the feedforward

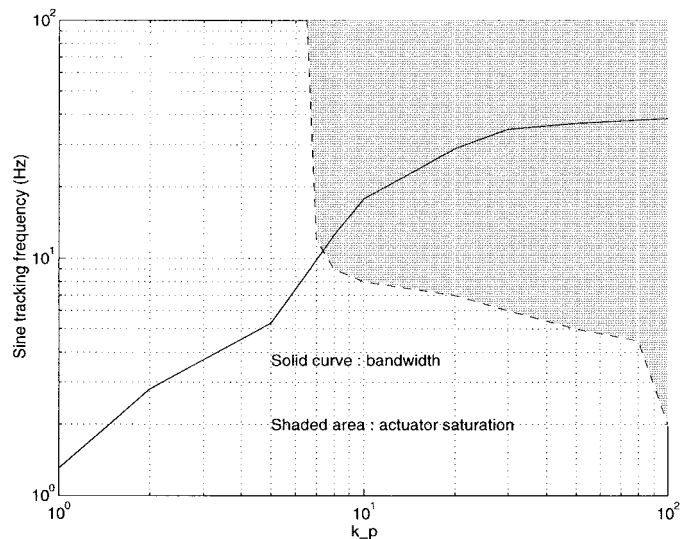


Fig. 14. Effect of gain and tracking frequency on the actuator saturation.

control output is

$$i = \frac{k_p}{k}(F_d - F_a) + f^{-1}(F_d) \quad (14)$$

The closed-loop frequency response of the actuator was tested with the aid of an HP 35665A dynamic signal analyzer, which provided the input to the control system and analyzed the output. Several time-domain, force tracking experiments were performed to examine the fidelity of the model and test different control strategies. In the following sections, we first explain some practical issues such as actuator saturation and servo rate selection. Then, we discuss frequency and time-domain force tracking.

A. Actuator Saturation

During force sine wave tracking, ripple was occasionally observed, which input voltage recordings indicate was due to actuator saturation. This saturation depends on feedback gain and tracking frequency.

Fig. 14 shows the result of several tests using feedforward control. The mean force is 45 N and the amplitude is 5 N. For other values of force mean and amplitude, the figure shows slight changes. The servo rate is 1 kHz. It is seen that as k_p increases, the -3 dB bandwidth increases (solid curve). For $k_p > 7.5$, even though the bandwidth increases, actuator saturation occurs and the force signal becomes noisy. The actuator never saturates for $k_p < 6.5$.

Fig. 14 permits informed selection of gain. For example, if we wish to track a 4 Hz sine force, we should use the maximum possible gain before saturation occurs. Fig. 14 suggests $k_p = 83$ for this case. On the other hand, if a small tracking error is desired for a step response, we may first select the minimum required gain from the step response experiments, then the maximum sine tracking frequency is easily obtained by Fig. 14. If that gain is more than 7.5, the limiting factor on the sine tracking frequency will be actuator saturation. Otherwise, the limiting factor will be the bandwidth curve (solid) of Fig. 14.

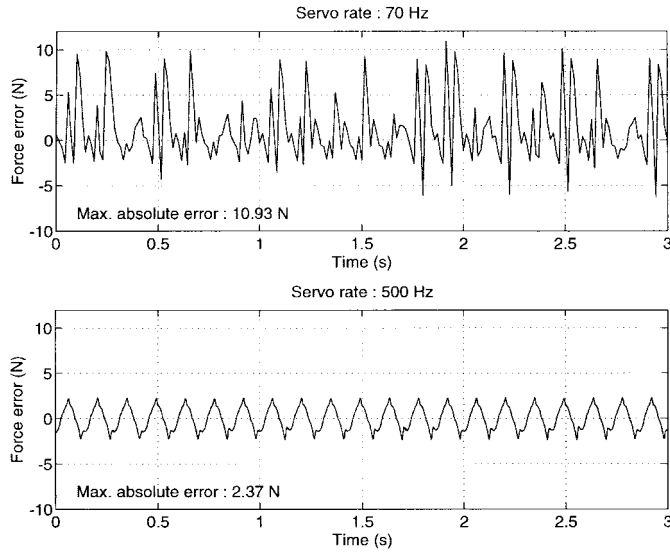


Fig. 15. Effect of servo rate on the sine force tracking error.

B. Choosing Servo Rates

Next we consider the selection of an appropriate servo rate, which in our scheme is equal to the sampling rate. Khosla [18] proposed a method based on system stability to find the maximum k_p and k_v with the maximum possible sampling rates. We do not use that method here, because we deal with saturation instead of stability problems. We implemented several servo rates with different gains. A typical result of the sine force tracking error is shown in Fig. 15 for a proportional feedback gain of 20. Fig. 14 suggests that the maximum tracking frequency before saturation is 7 Hz. This tracking frequency was used in Fig. 15. The mean force is 45 N and the amplitude is 5 N. It is seen that for a servo rate of 70 Hz, the tracking error can rise to 10.93 N. A servo rate of 500 Hz decreased the error to 2.37 N; further servo rate increases did not significantly improve the tracking error. In the rest of this paper, we used either 500 Hz or 1 kHz for experiments.

C. Frequency Response

Fig. 16 shows the effect of k_p on the frequency response. It is seen that as the gain increases, bandwidth increases. An interesting feature of Fig. 16 is that the slope of the magnitude plot is -20 dB as long as the actuator is not saturated (solid and dotted curves). This is a confirmation of results presented for the open loop dynamic characteristics in previous sections that the nonlinear system resembles mostly a first order linear system. On the other hand, when the actuator is saturated (dashdot and dashed curves), the magnitude plot shows a -40 dB slope. Thus, the saturated actuator cannot be modeled by a first order linear system. Fig. 14 helps find saturated curves in Fig. 16.

The magnitude plot for $k_p = 2$ does not start from 0 db. It is due to the dominance of hysteresis to the input control voltage for low gains.

The frequency response changes slightly with the mean and the amplitude of force. As an example, Fig. 17 shows the Bode plot for four different force amplitudes using $k_p = 30$.

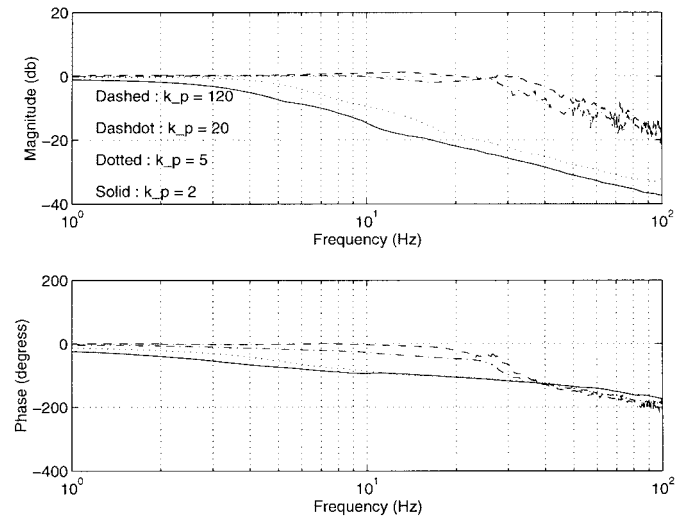


Fig. 16. Effect of gain on the frequency response.

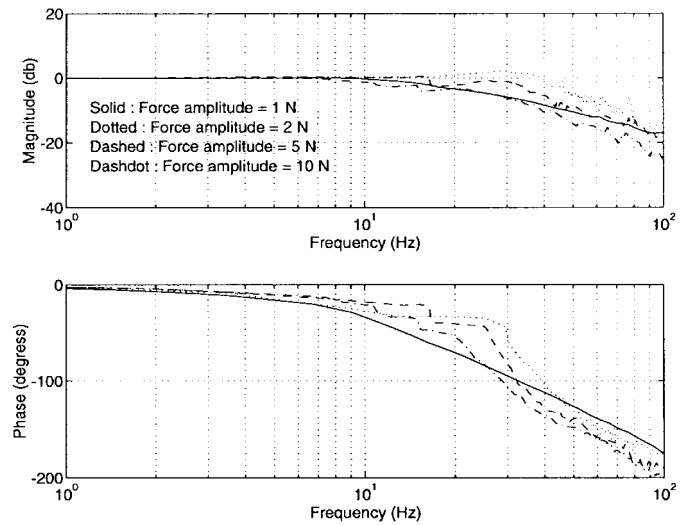


Fig. 17. Frequency response for different force amplitudes and a mean force of 45 N.

The amplitude of 1 N did not saturate the actuator. As the amplitude increases, the bandwidth increases to 46 Hz for a 2 N amplitude, and decreases again to 15 Hz for a 10 N amplitude. At high frequencies, phase constantly decreases. This behavior is also observed in the open loop force control of the actuator.

D. Time-Domain Force Tracking

Simulations were performed using a fourth-order Runge–Kutta integration [24]. The simulation method proceeds by casting the system differential equations (3) and (12) into nonlinear state-space form

$$\dot{\mathbf{x}} = \Theta(\mathbf{x}, u) \quad (15)$$

and integrating over a suitably small time period. In (15), $\mathbf{x} = [i \ \ddot{x}_{jp} \ \dot{x}_{jp} \ x_{jp} \ P_1 \ P_2]^T$ is the vector of state variables, u is the D/A input voltage, and Θ is the set of state equations. All the other relations, including the output actuator force, are

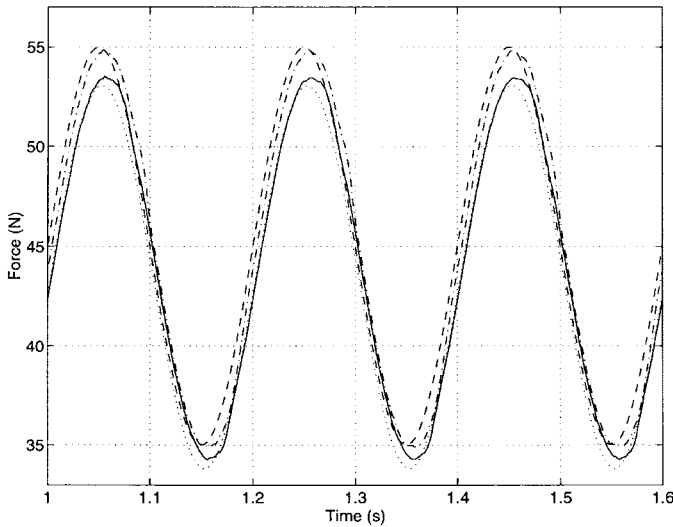


Fig. 18. Force tracking of a desired 5 Hz sine wave (dashed line) of proportional feedback control (solid) versus feedforward control (dashdot). Dotted line: modeled proportional control response.

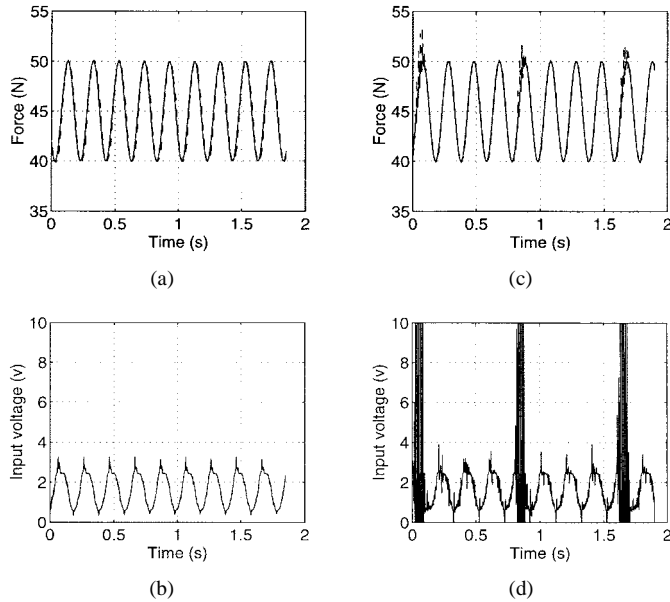


Fig. 19. Effect of actuator saturation on force tracking obtained by experiments.

static relations and hence are obtained at any time from the corresponding state variables.

The experimental results in Fig. 18 show that the performance of proportional feedback control is good, but there is an offset that is significantly reduced by feedforward control. Raising the feedback gain can reduce the offset, but can also lead to actuator saturation and instability. Also shown is the good correlation between the model and experimental data for proportional feedback control.

The effect of actuator saturation on 5-Hz force tracking under feedforward control was determined experimentally and is shown in Fig. 19(a) for $k_p = 30$ and in Fig. 19(c) for $k_p = 80$. Fig. 19(b) and (d) show the corresponding input voltages. The actuator saturation shown in 19(d) causes noise at the corresponding points in 19(c). Obviously, such a high gain

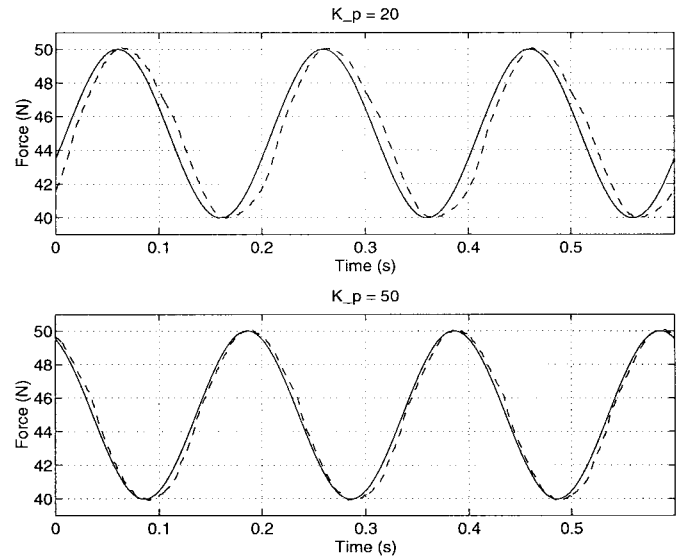


Fig. 20. Effect of gain on force tracking (solid: desired force; dashed: actual force). Maximum absolute error is 1.97 N for $k_p = 20$ and 0.89 N for $k_p = 50$.

is not acceptable. This result could also be understood from Fig. 14.

Fig. 20 shows the effect of gain on tracking a 5 Hz sine force using feedforward control. It is seen that the tracking error decreases considerably with higher gains. From Fig. 14, we realize that $k_p = 50$ is the maximum possible gain for tracking this frequency before saturation occurs.

V. LINEAR ANALYSIS

A. Closed-Loop Frequency Response

A linear analysis was performed to explain the improvement using proportional feedback control (Fig. 12). If the plant dynamics are approximated by a first-order linear model, as open-loop frequency response tests and the linear analysis of Section V-B suggest, the closed-loop response of the system using a feedback gain of k_p can be determined as

$$\text{plant dynamics: } P(s) = \frac{F_a(s)}{I(s)} = k \left(\frac{a}{s+a} \right)$$

$$\text{controller: } i = \frac{k_p}{k} e = \frac{k_p}{k} (F_d - F_a)$$

$$\text{system dynamics: } \frac{F_a(s)}{F_d(s)} = \frac{k_p a}{s+a+k_p a}$$

where a is the plant open-loop bandwidth. The system bandwidth has been raised from a to $a + k_p a$. The steady state gain is $k_p a / (a + k_p a)$, which is marginally less than unity. Systems with a large value of k can benefit enormously from even small feedback gains. A quick check of Fig. 9(a) or 10 reveals that $k \approx 550$ N/A, which is large indeed.

In Section III-B, we concluded that the measured open-loop system bandwidth a is 0.8–2.8 Hz for small perturbations about a 45 N output force operating point. Using this value, and the value of the feedback gains used in the closed-loop force control experiments, the theoretical closed-loop bandwidth

TABLE II
POLES AND ZEROS (RAD/S) OF LINEARIZED ACTUATOR MODEL FOR
ACTUATOR FORCE OF 45 N WITH PLSTON AT MID-STROKE POSITION

Element	Zero	Pole
current driver		-7049.7
jet pipe		-973.9
		$-35.3 \pm 1856.3j$
fluid dynamics	-7.1	-5.0
		-14.5

$\omega_{cl} = a + k_p a$ for the linear system can be computed

$$0.8 + 0.8k_p \leq \omega_{cl} \leq 2.8 + 2.8k_p \quad (16)$$

where $0.8 \text{ Hz} \leq a \leq 2.8 \text{ Hz}$. This value agrees well with the experimentally observed bandwidth in Fig. 14. Although the theoretical closed-loop system is stable for all positive feedback gains, in practice, actuator saturation, sensor noise, and unmodeled dynamics limit the size of the gain that can be used.

B. Linearized Model

To gain some qualitative insight into the parameters that influence the response of the actuator and model, a linear analysis of the current driver, jet pipe, and fluid flow equations was performed for small perturbations about a nominal set operating conditions. The poles and zeros of the linearized system for operating conditions corresponding to an actuator output force of 45 N and stopper position of 54 mm are shown in Table II. The current driver contributes to a pole because it is a low pass first order system. Three poles are due to the jet pipe as described in Section II-B. Two more poles are due to fluid dynamics at chambers 1 and 2 (12). Thus, a sixth order linear model is obtained. The description of state space model is found in [9]. The single zero at 1.1 Hz (7.1 rad/s) contributed by the fluid dynamics is located close to the pole at 0.8 Hz (5.0 rad/s) and therefore effectively cancels this term out. Although this model is sixth-order, the remaining pole due to the fluid dynamics is at a low frequency of 2.3 Hz (14.5 rad/s) and hence dictates the overall system response. Therefore, the actuator, at this operating point, tends to behave like a first-order, low-pass system with a corner frequency of 2.3 Hz. This frequency compares well with the observed range of 0.8–2.8 Hz described in Section III-B. Since there is a large amount of hysteresis in the actuator force/current relationship, there is no single current which corresponds to a given actuator output force. Therefore comparison between the experimental, open-loop, force/current frequency response and the theoretical response which excludes hysteresis is only qualitative.

To investigate the effect of the operating point of the linearized model on the open-loop bandwidth, the bandwidth was obtained as a function of the rod stopper position x_s at several different actuator output forces F_{act} (Fig. 21). The results show that the open-loop bandwidth is inversely proportional to the chamber 1 volume and increases with actuator output force. The latter behavior was observed during experimental frequency response tests performed on the actuator (Section III-B).

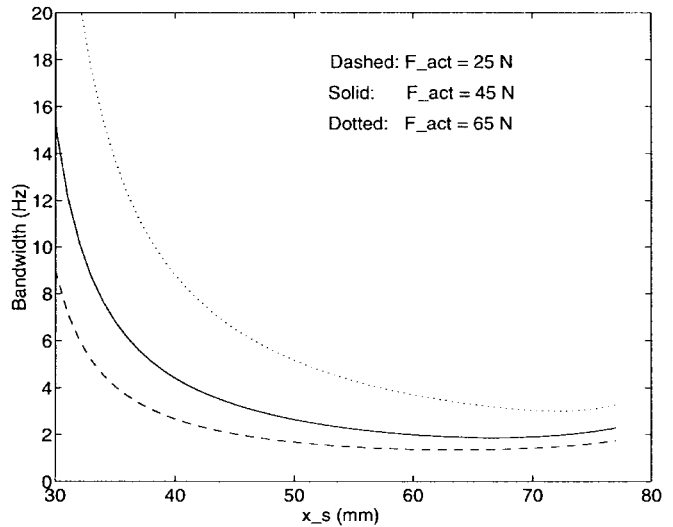


Fig. 21. Effect of operating point on actuator open-loop bandwidth.

The information obtained by linearizing the model for a variety of operating points can be used by the control system to aid in the selection of feedback gains, and in the analysis of stability. For example, a function could be derived relating stopper position and actuator force to open-loop bandwidth. Since the piston rods are directly connected to the robot finger joint via the tendons, the stopper position could easily be calculated using joint angle information. These parameters could be monitored by the control system in real time and feedback gains dynamically adjusted to obtain a constant level of performance regardless of the operation.

C. Comparison With Nonlinear Actuator Model

The performance of the linearized model was examined by comparing force-control simulations using the linearized and nonlinear models with experimental data. A set of nominal conditions for the linearized model was selected corresponding to the same experimental conditions: $F_{act} = 45 \text{ N}$, $x_s = 54 \text{ mm}$. Fig. 22 compares simulations using the linearized and nonlinear models for proportional feedback control. The results show a high degree of correlation between the two models and the experimental data. Nonetheless, the linearized model is shown to perform as well as the nonlinear model at this operating point.

The linearized model is only valid for small perturbations about the given operating point, and therefore can be expected to perform poorly for different conditions. For instance, the orifice area functions and jet pipe saturation regions introduce nonlinearities, which are not adequately accounted for with a single operating point. Linearizing the model for a variety of operating points (Fig. 21) shows that the open-loop bandwidth varies significantly with stopper position and actuator force. To overcome this fundamental problem with linearized models, time-varying models can be used to essentially move the operating point as the operating conditions change. Of course this requires the existence of a nonlinear model to begin with, a fact that further reinforces the value of a detailed nonlinear model.

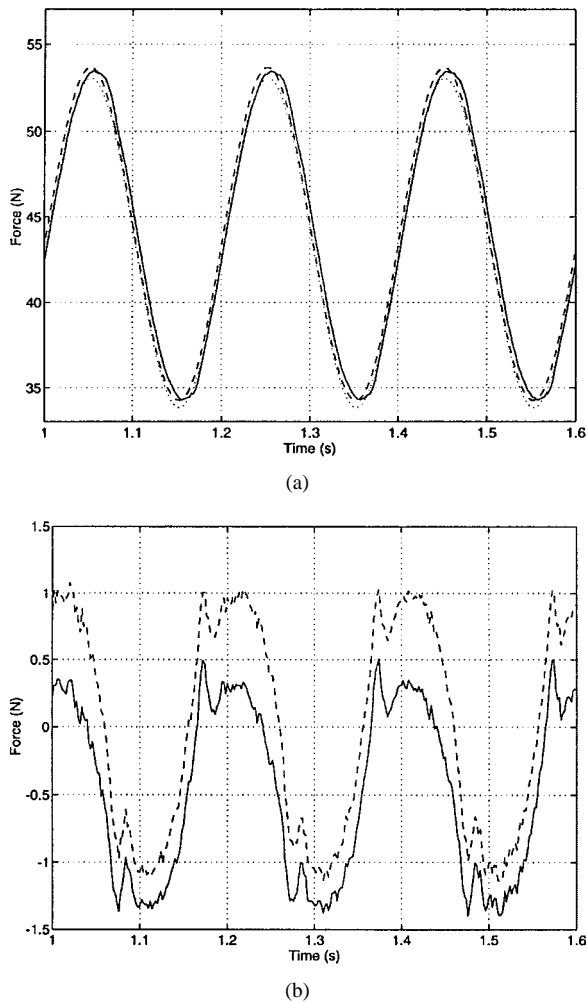


Fig. 22. (a) Comparison between linearized and nonlinear model for tracking 5 Hz sine wave for the proportional controller. solid: actual; dashed: linearized model; dotted: nonlinear model. (b) Error between model and experimental data. solid: nonlinear model; dashed: linearized model.

VI. CONCLUSION

An analytical and experimental investigation of a jet pipe controlled pneumatic actuator was performed. A nonlinear dynamic model including a detailed representation of the jet pipe element, orifice areas and fluid flows was developed and was shown to predict the response of the actuator well.

Experimental analysis of the jet pipe showed a significant amount of hysteresis. Further study revealed the main source of hysteresis to be a nonlinear mechanical effect in the jet pipe rather than the magnetic flux of the coil.

Open-loop frequency response testing of the actuator revealed that the system response approaches that of an integrator, and that the bandwidth can be increased substantially with closed-loop control. Experimental results showed that saturation is an obstacle for high bandwidth. If we neglect saturation, a bandwidth as high as 40 Hz is attainable. The maximum bandwidth for a nonsaturated actuator is 10 Hz.

Further work related to the actuator model might involve refinement of the fluid flow portion of the model to explicitly account for the clearance between the jet pipe tip and the receiver plate. Furthermore, all actuator testing was performed

with the piston held stationary. Although the model works well under this condition, dynamic testing would permit the study of friction inside the cylinder and possible rate limits due to finite flow from the valve.

Implementation of model-based control on the Utah/MIT Dextrous Hand necessitates the modeling of all the subsystems including actuators, tendon transmission system, finger kinematic and inertial parameters, and sensors. Research is currently underway to characterize the tendon transmission system, including the effects of tendon dynamics and pulley friction [22], with future plans directed toward kinematic calibration [4]. Model-based control is a large and complex issue and should be investigated in a systematic and careful manner.

Other control strategies could also be investigated. Xu *et al.* [29] present a nonmodel-based, nonlinear PD controller which actively raises the damping and stiffness when the motion is in an unfavorable direction. This controller, which is related to the original analog controller designed for the UMDH [14], is easy to implement and would permit very fast servo rates.

ACKNOWLEDGMENT

The authors would like to thank I. Hunter for suggestions regarding the instrumentation.

REFERENCES

- [1] P. K. Allen and P. Michelman, "Acquisition and interpretation of 3-D sensor data from touch," *IEEE Trans. Automat. Robot.*, vol. 6, pp. 397-404, 1990.
- [2] B. W. Andersen, *The Analysis and Design of Pneumatic Systems*. New York: Krieger, 1976.
- [3] D. Ben-Dov and S. E. Salcudean, "A force-controlled pneumatic actuator," *IEEE Trans. Robot. Automat.*, vol. 11, pp. 906-911, 1995.
- [4] D. J. Bennett and J. M. Hollerbach, "Closed-loop kinematic calibration of the Utah-MIT hand," *Experimental Robotics I—The First International Symposium*, V. Hayward and O. Khatib, Eds. New York: Springer-Verlag, 1990, pp. 539-552.
- [5] J. F. Blackburn, G. Reethof, and J. L. Shearer, *Fluid Power Control*. Cambridge, MA: MIT Press, 1960.
- [6] B. Boulet, L. Daneshmend, V. Hayward, and C. Nemri, "System identification and modeling of a high performance hydraulic actuator," in *Experimental Robotics II—The Second International Symposium*, R. Chatila and G. Hirzinger, Eds. New York: Springer-Verlag, 1992.
- [7] C. R. Burrows, "Effect of position on the stability of pneumatic servomechanisms," *J. Mech. Eng. Sci.*, vol. 11, pp. 615-616, 1969.
- [8] J. G. Frame, N. Mohan, and T. Liu, "Hysteresis modeling in an electromagnetic transients program," *IEEE Trans. Power Appar. Syst.*, vol. PAS-101, pp. 3403-3411, 1982.
- [9] P. D. Henri, *Study of a Jet Pipe Electropneumatic Actuator*, Rep., Dept. Biomedical Eng., McGill Univ., Montreal, P.Q., Canada, 1994.
- [10] P. D. Henri and J. M. Hollerbach, "An analytical and experimental investigation of a jet pipe controlled electropneumatic actuator," in *Proc. IEEE Int. Conf. Robot. Automat.*, 1994, pp. 300-306.
- [11] J. M. Hollerbach, I. W. Hunter, and J. Ballantyne, "A comparative analysis of actuator technologies for robotics," *Robotics Review 2*, O. Khatib, J. J. Craig, and T. Lozano-Perez, Eds. Cambridge, MA: MIT Press, 1992, pp. 299-342.
- [12] M. Huber and R. A. Grupen, "2-D contact detection and localization using proprioceptive information," *IEEE Trans. Robot. Automat.*, vol. 10, pp. 23-33, 1994.
- [13] S. C. Jacobsen, F. M. Smith, D. K. Backman, and E. K. Iversen, "High performance, high dexterity, force reflective teleoperator II," *ANS Topical Meeting Robot. Remote Syst.*, Albuquerque, NM, Feb. 24-27, 1991.
- [14] S. C. Jacobsen, J. E. Wood, D. F. Knutti, and K. B. Biggers, "The Utah/MIT dextrous hand: Work in progress," *Int. J. Robot. Res.*, vol. 3, no. 4, pp. 21-50, 1984.

- [15] S. C. Jacobsen, D. F. Knutti, K. B. Biggers, E. K. Iversen, and J. E. Wood, "An electropneumatic actuation system for the Utah/MIT dextrous hand," *Theory Practice Robot Manipulators, Proc. RoManSy'84: 5th CISM/IFTOMM Symp.*, 1984, pp. 271–279.
- [16] S. C. Jacobsen, E. K. Iversen, D. F. Knutti, R. T. Johnson, and K. B. Biggers, "Design of the Utah/MIT dextrous hand," in *Proc. IEEE Int. Conf. Robot. Automat.*, 1986, pp. 1520–1534.
- [17] Y. Kawakami, J. Akao, and S. Kawai, "Some considerations on the dynamic characteristics of pneumatic cylinders," *J. Fluid Contr.*, vol. 75, pp. 22–36, 1988.
- [18] P. K. Khosla, "Choosing sampling rates for robot control," in *Proc. IEEE Intl. Conf. Robot. Automat.*, 1987, pp. 69–174.
- [19] S. Liu and J. E. Bobrow, "An analysis of a pneumatic servo system and its application to a computer-controlled robot," *J. Dyn. Syst., Meas., Contr.*, vol. 110, pp. 228–235, 1988.
- [20] T. W. McLain, E. K. Iversen, C. C. Davis, and S. C. Jacobsen, "Development, simulation and validation of a highly nonlinear hydraulic servosystem model," in *Proc. Amer. Contr. Conf.*, 1989, pp. 385–391.
- [21] F. Mougnet and V. Hayward, "Limit cycle characterization, existence and quenching in the control of a high performance hydraulic actuator," *IEEE Int. Conf. Robot. Automat.*, 1995, pp. 2218–2223.
- [22] A. Nahvi, J. M. Hollerbach, Y. Xu, and I. W. Hunter, "An investigation of the transmission system of a tendon driven robot hand," in *Proc. IEEE/RSJ Intl. Conf. Intell. Robot Syst.*, 1994, pp. 202–208.
- [23] S. Narasimhan, D. M. Siegel, and J. M. Hollerbach, "Condor: An architecture for controlling the Utah-MIT dextrous hand," *IEEE Trans. Robot. Automat.*, vol. 5, pp. 616–627, 1989.
- [24] W. H. Press, S. A. Teukolsky, W. T. Vetterling, and B. P. Flannery, *Numerical Recipes in C*. Cambridge, U.K.: Cambridge Univ. Press, 1992.
- [25] R. N. Rohling, J. M. Hollerbach, and S. C. Jacobsen, "Optimized fingertip mapping: A general algorithm for robotic hand teleoperation," *Presence: Teleoperat. Virtual Environ.*, vol. 2, pp. 203–220, 1993.
- [26] J. L. Shearer, "Study of pneumatic processes in the continuous control of motion with compressed air—I and II," *Trans. ASME*, pp. 233–249, Feb. 1956.
- [27] ———, "Digital simulation of a Coulomb-damped hydraulic servosystem," *J. Dyn. Syst., Meas., Contr.*, vol. 105, pp. 215–221, Dec. 1983.
- [28] W. J. Thayer, *Electropneumatic Servoactuation: An Alternative to Hydraulics for Some Low Power Applications*, Moog Tech. Bull. 151, East Aurora, NY, 1984.
- [29] Y. Xu, J. M. Hollerbach, and D. Ma, "A nonlinear PD controller for force and contact transient control," *IEEE Contr. Syst.*, vol. 15, no. 1, pp. 15–21, 1995.



John M. Hollerbach (M'85–SM'92–F'96) received the B.S. degree in chemistry and the M.S. degree in mathematics, both from the University of Michigan, Ann Arbor, in 1968 and 1969, respectively, and the S.M. and Ph.D. degrees in computer science, both from the Massachusetts Institute of Technology (MIT), Cambridge, in 1975 and 1978, respectively.

He is Professor of Computer Science and Research Professor of Bioengineering and of Mechanical Engineering, University of Utah, Salt Lake City. From 1989 to 1994, he was the Natural Sciences and

Engineering/Canadian Institute for Advanced Research Professor of Robotics at McGill University, Montreal, P.Q., Canada, jointly in the Departments of Mechanical Engineering and Biomedical Engineering. From 1982 to 1989, he was on the faculty of the Department of Brain and Cognitive Sciences and a member of the Artificial Intelligence Laboratory, MIT. From 1978 to 1982 he was a Research Scientist. His research interests combine robotics, human motor control, teleoperation, virtual reality, and microelectromechanical systems.

Dr. Hollerbach received an NSF Presidential Young Investigator Award in 1984 and was named a Fellow of the Canadian Institute for Advanced Research in 1988. He was the Program Chairman of the 1989 IEEE International Conference on Robotics and Automation, a member of the Administrative Committee of the IEEE Robotics and Automation Society from 1989 to 1993, Technical Editor of the IEEE TRANSACTIONS ON ROBOTICS AND AUTOMATION from 1989 to 1994, and Treasurer of the IEEE/ASME *Journal of Microelectromechanical Systems* from 1992 to 1997. He was a member of the 1994–1995 National Research Council Committee on Virtual Reality Research and Development. Presently he is a Senior Editor of *Presence: Teleoperators and Virtual Environments*, an Editorial Board member of the *International Journal of Robotics Research*, and a Governing Board member of the electronic journal *Haptics-e*.

Ali Nahvi, photograph and biography not available at the time of publication.



Paul D. Henri received the B.Eng. degree in mechanical engineering and the M.Eng. in biomedical engineering from McGill University, Montreal, P.Q., Canada, in 1989 and 1994, respectively.

He is a Senior Designer at Nortel, Ottawa, Ont., Canada, in the area of advanced internetwork-layer routing and switching over ATM.